THE JOURNAL OF PHYSICAL CHEMISTRY C

Article

pubs.acs.org/JPCC

Robust Phase Control through Hetero-Seeded Epitaxial Growth for Face-Centered Cubic Pt@Ru Nanotetrahedrons with Superior Hydrogen Electro-Oxidation Activity

Jun Gu,[†] Yu Guo,[†] Ying-Ying Jiang,[‡] Wei Zhu,[†] Yan-Shuang Xu,[†] Ze-Qiong Zhao,[†] Jin-Xun Liu,[§] Wei-Xue Li,*[,§] Chuan-Hong Jin,[‡] Chun-Hua Yan,[†] and Ya-Wen Zhang*[,†]

[†]Beijing National Laboratory for Molecular Science, State Key Laboratory of Rare Earth Materials Chemistry and Applications, PKU-HKU Joint Laboratory in Rare Earth Materials and Bioinorganic Chemistry, College of Chemistry and Molecular Engineering, Peking University, Beijing 100871, P. R. China

[‡]State Key Laboratory of Silicon Materials, Key Laboratory of Advanced Materials and Applications for Batteries of Zhejiang Province and School of Materials Science and Engineering, Zhejiang University, Hangzhou, Zhejiang 310027, P. R. China

[§]State Key Laboratory of Catalysis, Dalian Institute of Chemical Physics, Chinese Academic of Sciences, Dalian 116023, P. R. China

Supporting Information

ABSTRACT: Controllable synthesis of metallic nanocrystals (NCs) with tunable phase, uniform shape, and size is of multidisciplinary interests but has still remained challenging. Herein, a robust phase control strategy is developed, in which seeds with a given phase are added to guide the epitaxial growth of the target metal to inherit the seeds' phase. Through this strategy, M@Ru (M = Pt, Pd) NCs in the face-centered cubic (*fcc*) phase, a metastable phase for Ru under ambient conditions, were synthesized with the hydrothermal method. The Pt@Ru NCs showed not only the pure *fcc* phase but also high morphology selectivity to tetrahedrons surrounded by {111} facets. As revealed by density function theory (DFT) calculations, the preferentially epitaxial growth of Ru atom layers on the nonclosest-packed facets of hetero *fcc* metal seeds led to the formation of *fcc* Ru shells. Furthermore, the *fcc* Pt@Ru tetrahedrons/C showed electrocatalytic activity enhancement with more than an order of magnitude toward hydrogen oxidation reaction (HOR) in acidic electrolyte compared with hydrothermally synthesized Ru/C. Electrochemical measurement combined with DFT calculations revealed that the optimum HOR activity should be achieved on well-crystallized *fcc* Ru catalysts exposing maximum {111} facets.

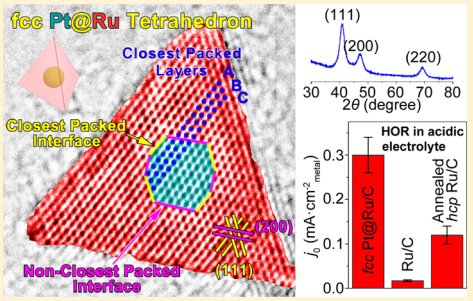

The surface atomic arrangement of metallic nanocatalysts, which strongly affect the interaction between the substrate molecules and the catalysts' surface, and consequently their catalytic performance, is determined by both their phase and exposing facets. For instance, face-centered cubic (*fcc*) Ru nanocrystals (NCs) show higher catalytic activity to CO oxidation than hexagonal closest packed (*hcp*) ones, because *fcc* NCs exposed more the closest packed surface of Ru which exhibit higher activity to this reaction.[1,2] *hcp* Co NCs exhibited higher catalytic activity toward Fischer−Tropsch synthesis than *fcc* ones[3,4] since the {10−11} facets of *hcp* Co comprise active sites for CO activation.[5] *hcp* Co NCs exposing more {10−11} facets would predictably represent even higher activity. The exposing-facet-control, namely the shape-control synthesis of metallic NCs, has been widely investigated during the past decade, and the development of phase control strategies is attracting increasing attention.[1,2,6−10] The existing strategies to tune the phase of metallic NCs contain decreasing particle size,[2,6] varying composition,[7,8] introducing supports,[9] and using an intermediate compound to link up a phase transition.[3,10] However, through these strategies, it remains difficult to prepare metallic NCs in the metastable phase together with good crystallinity and uniform shape. Therefore, more robust phase control strategies of metallic NCs are still in demand.

Introducing metal seeds with a given phase is a possible route to prepare core−shell NCs with shells inheriting the seeds' phase. Recently, a great deal of research attention was drawn to the heteronanostructures combined metals with different phases.[11−16] For instance, Ru shows an *hcp* structure under ambient conditions, different from Pt, Pd, Rh, etc. which show an *fcc* structure.[17] As reported by Eichhorn and co-workers, when Pt shells were grown on highly distorted *hcp* Ru cores, the Pt shells retained the *fcc* phase with the disordered Pt−Ru interface.[12] In the work of Wang and co-workers, when Pt atoms were epitaxially deposited on well crystallized *hcp* Ru NCs, the *hcp*-to-*fcc* transition across the Ru (0001)−Pt (111) interface was observed.[14] In these cases, the shell metal maintained its bulk phase rather than followed the seeds' phase.

In this work, we developed a new phase control strategy of metallic NCs, whereby heterometal seeds were introduced to

Received: May 13, 2015
Revised: July 18, 2015
Published: July 21, 2015

DOI: 10.1021/acs.jpcc.5b04587
J. Phys. Chem. C 2015, 119, 17697−17706

guide a target metal adopting the seeds' phase, a phase difficult to achieve under ambient conditions for this target metal itself, via epitaxial growth during the hydrothermal synthesis. When *fcc* Pt or Pd NCs were introduced as seeds for the growth of Ru shells, well crystallized *fcc* M@Ru (M = Pt, Pd) NCs were obtained. According to XRD data fitting, the phase selectivity of *fcc* Ru exceeded 90% as long as 10 at. % Pt was introduced. The interface models of Ru ad-layers on various facets of *fcc* metals (Pt, Pd, Rh) show that the epitaxial deposition of Ru atoms on the nonclosest-packed facets of the *fcc* metal necessarily lead to the formation of *fcc* Ru layers. Moreover, the density function theory (DFT) calculations suggested the interface between the nonclosest-packed facets of *fcc* metals and Ru is thermodynamically more favored, which further facilitates the generation of *fcc* Ru shells. More importantly, shape control was realized together with phase control in our method. The obtained *fcc* Pt@Ru NCs showed uniform tetrahedral morphology enclosed by {111} facets of *fcc* Ru, due to the relatively low surface energy and the selective adsorption of water and oxalate on these facets.

The carbon black supported *fcc* Pt@Ru nanotetrahedrons served as highly active electrocatalysts toward hydrogen oxidation reaction (HOR) in acidic electrolyte, the anodic half reaction of proton exchange membrane fuel cell (PEMFC).[18−22] The HOR specific activity of the most active sample was 18 times that of hydrothermally synthesized poorly crystallized Ru nanospheres (NSs)/C and 2.5 times that of the *hcp* Ru NSs/C annealed at 500 °C, indicating that the phase and crystallinity of the Ru catalysts have great influence on their catalytic performance. Moreover, DFT calculation was used to help us to understand how the crystallinity, phase, and exposing facets of the Ru catalyst influence the catalytic activity toward HOR. HOR catalysts with high activity should have moderate adsorption energy of hydrogen.[23] The calculation results showed the surfaces of amorphous Ru NCs and the open facets of the Ru crystal tend to be partially passivated by oxygen at the potential for HOR and the adsorption of hydrogen is too weak on these surfaces, while {111} facets of *fcc* Ru are more inert to the adsorption of oxygen and show moderate adsorption energy of hydrogen. The *fcc* Pt@Ru nanotetrahedrons maximized the exposure of {111} facets of *fcc* Ru, and, consequently, greatly enhanced HOR activity was achieved on this kind of nanocatalysts.

RESULTS AND DISCUSSION

The *fcc* Pt@Ru NCs were synthesized with a one-step hydrothermal method, in which K_2PtCl_4 and $RuCl_3$ were reduced by formaldehyde (HCHO) at 160 °C in the presence of sodium oxalate ($Na_2C_2O_4$), HCl, and poly(vinylpyrrolidone) (PVP). The samples were referred to as $Pt_x@Ru_{100-x}$, in which x was the molar percentage of Pt in the feedstock. Figure 1 shows the transmission electron microscopy (TEM) characterization of $Pt_{10}@Ru_{90}$. This sample was mainly composed of tetrahedrons (shape selectivity = 83%) with an average size of 8.3 nm (more than 200 particles were counted). Figure 1b-d shows the high resolution TEM (HRTEM) images and corresponding fast Fourier transition (FFT) patterns of $Pt_{10}@Ru_{90}$ tetrahedrons from [110], [100], and [112] zone axes, respectively, which are in good accord with the models of *fcc* tetrahedrons from each zone axes, explicitly indicating that these particles are *fcc* tetrahedral single crystals enclosed by {111} facets. Figure 1e and 1g show the high angular annular dark field-scanning transmission electron microscopy

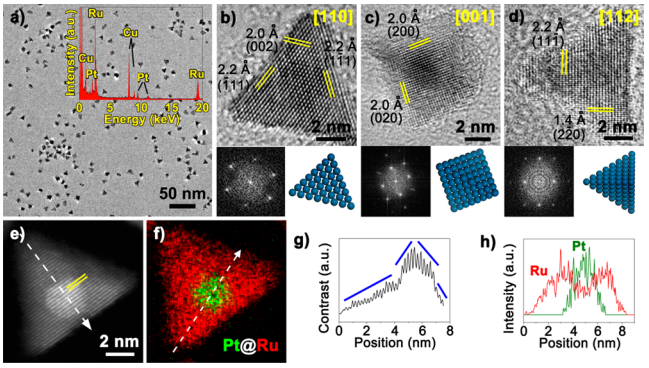

Figure 1. TEM characterization of the $Pt_{10}@Ru_{90}$ nanotetrahedrons. (a) TEM image and EDS spectrum. (b-d) HRTEM images, corresponding FFT patterns, and models of *fcc* tetrahedrons from [110], [100], and [112] zone axes, respectively. (e) HAADF-STEM image and (f) the corresponding EDS mapping. The yellow lines in panel (e) indicate the core and the shell share the same lattice distance. Green and red in panel (f) show the regions of Pt and Ru, respectively. (g) The contrast line profile along the white dashed arrow in panel (e). (h) The EDS line profiles of Pt (green) and Ru (red) along the white dashed arrow in panel (f).

(HAADF-STEM) image and corresponding contrast line profile. The contrast increased gradually from the edges to the center of the particle, confirming that tetrahedrons rather than triangular plates were obtained. A rounded high-contrast region is shown in the center, corresponding to the Pt core of the particle. Furthermore, the X-ray energy dispersive spectroscopy (EDS) mapping (Figure 1f) and line profile (Figure 1h) of this particle clearly show the Pt@Ru core−shell structure with rounded Pt core and compact Ru shell. Only one set of lattice fringes can be seen in each HRTEM and HAADF-STEM image (Figure 1b-1e), and no Moire fringes were observed, indicating that the Ru shells were epitaxially grown on all of the exposing surface of *fcc* Pt cores, and the Pt cores and the Ru shells shared the same lattice parameter.

Pt@Ru NCs with other compositions were synthesized by changing the feeding ratio of K_2PtCl_4 and $RuCl_3$. EDS and inductively coupled plasma atomic emission spectroscopy (ICP-AES) analyses showed that the Pt:Ru ratio of all samples agreed well with the loading ratio between two metals (Table S1), indicating both precursors were reduced completely. Figure S1 shows the TEM and HRTEM images of $Pt_5@Ru_{95}$, $Pt_{20}@Ru_{80}$, and $Pt_{50}@Ru_{50}$. Similar to $Pt_{10}@Ru_{90}$, $Pt_5@Ru_{95}$, and $Pt_{20}@Ru_{80}$ were mainly composed of tetrahedral single crystals enclosed by {111} facets, and $Pt_{50}@Ru_{50}$ comprised single-crystalline octahedrons and truncated ones. The average size of Pt@Ru NCs (defined as the distance from a vertex to the opposite base plane for tetrahedrons and the length between two parallel surfaces for NCs in $Pt_{50}@Ru_{50}$) decreased from 10.5 to 5.9 nm as the Pt content increased from 5 at. % to 50 at. % (Figure S2). As indicated by HAADF-STEM and EDS mapping images (Figure S3), all samples showed the Pt@Ru core−shell structure with rounded Pt cores and compact Ru shells. For $Pt_{10}@Ru_{90}$ in Figure 1f, the thickness of Ru shells varied from ∼1 nm at the centers of triangular surfaces to ∼4 nm at corners, and the shell thickness decreased as the Ru content decreased (Figure S3).

Figure 2 shows the XRD refinement of Pt@Ru NCs with different compositions, and the fitting results were listed in Table 1. Three phases, *fcc* Ru, *fcc* Pt, and *hcp* Ru, were included in the refinement, and the lattice parameters of *fcc* phases were

DOI: 10.1021/acs.jpcc.5b04587
J. Phys. Chem. C 2015, 119, 17697−17706

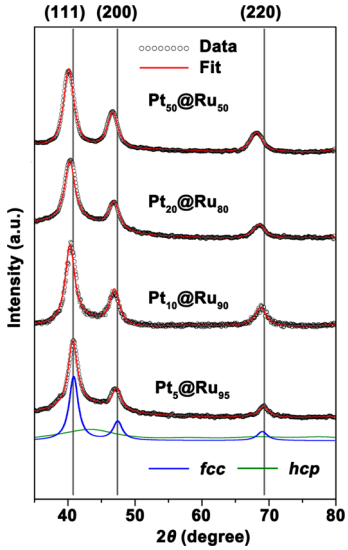

Figure 2. XRD data (circles) and Rietveld refinement (red lines) of Pt@Ru NCs with different Pt:Ru ratios. The contribution of the *fcc* phase and the *hcp* phase to the spectrum of $Pt_5@Ru_{95}$ were shown as blue and green lines, respectively. The gray vertical lines indicate the standard diffraction peaks of *fcc* Ru (No. 88-2333).

Table 1. Rietveld Analysis of Pt@Ru NCs with Different Pt:Ru Ratios

sample	phase	lattice constant (nm)	wt %
$Pt_5@Ru_{95}$	*fcc* Pt	3.838(8)	9
	fcc Ru	3.831(4)	73
	hcp Ru		18
$Pt_{10}@Ru_{90}$	*fcc* Pt	3.854(6)	17
	fcc Ru	3.850(6)	76
	hcp Ru		7
$Pt_{20}@Ru_{80}$	*fcc* Pt	3.860(9)	30
	fcc Ru	3.857(8)	66
	hcp Ru		4
$Pt_{50}@Ru_{50}$	*fcc* Pt	3.900(4)	57
	fcc Ru	3.898(6)	40
	hcp Ru		3

allowed to relax. Figure S4 summarized the contribution of each phase and the detailed fitting parameters. The contribution of *hcp* Ru mainly appeared as a very broad peak around 44° (green line for *hcp* Ru composition of $Pt_5@Ru_{95}$ in Figure 2), suggesting that poorly crystallized *hcp* Ru NCs might coexist in the sample. The contribution of *hcp* Ru decreased as the amount of *fcc* Pt cores increased, and the selectivity of the *fcc* phase was higher than 90% as long as the content of Pt was higher than 10 at. %. The fitted lattice parameters of *fcc* Ru and *fcc* Pt were quite close for each sample, in accordance with the HRTEM observation that the Pt cores and Ru shells share the same lattice parameter. Since the lattice constant of *fcc* Pt (a = 3.93 Å) is larger than that of *fcc* Ru (a = 3.83 Å, calculated[24]), Pt cores were compressed and Ru shells extended, and as the Pt content increased, the lattice parameters of core−shell NCs increased.

The evolution of Pt@Ru NCs during the one-step hydrothermal synthesis was monitored by TEM and ICP-AES characterizations, as shown in Figure 3a-c. The Pt precursor was reduced rapidly, and rounded Pt nanosingle-crystals formed in the first 0.5 h. The reduction efficiency of Pt

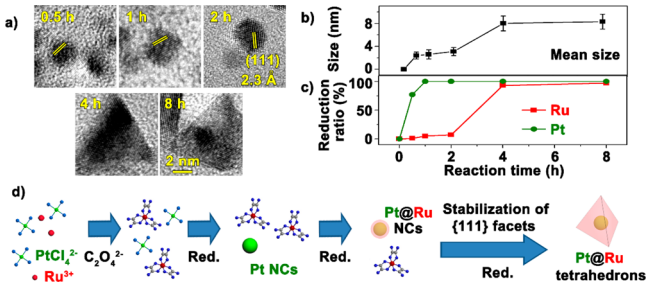

Figure 3. Monitoring of the NCs evolution during the synthesis of $Pt_{10}@Ru_{90}$. (a) HRTEM images, (b) mean size of the NCs, and (c) the reduction efficiency of Pt and Ru obtained from ICP-AES at different reaction times. All the images in panel (a) share the same scale bar. The (111) lattice fringes of *fcc* Pt cores were labeled in the first three images. (d) Scheme of the formation mechanism of Pt@Ru NCs in one-step synthesis.

reached 100% within 1 h, while the Ru precursor was almost unreduced during the first 2 h, and the particle size maintained around 3 nm from 0.5 to 2 h. The reduction efficiency of Ru rose to ~100% from 2 to 4 h together with the increase in particle size, corresponding to the growth of Ru shells on the as-formed Pt seeds. The size and composition of the Pt@Ru NCs became stable in the period from 4 to 8 h. The above phenomena indicated that the formation of Pt@Ru NCs followed the seeded growth process, as summarized in Figure 2d. $C_2O_4^{2-}$ ions and Ru^{n+} ions (n = 2, 3) could form stable complexes,[25] and the reduction rate was essentially slowed down.[26] Therefore, the generation of Pt^0 and Ru^0 monomers was totally separated in time. Pt NCs formed first followed by the formation of Ru shells, which inherited the *fcc* structure of the Pt cores. The slow forming rate of Ru^0 monomers also avoided the self-nucleation of Ru atoms and facilitated the epitaxial growth. When presynthesized Pt cores were introduced instead of those formed *in situ*, as denoted as a two-step method, similar *fcc* Pt@Ru NCs were obtained, as shown by Figure S5.

It is interesting that the rounded Pt seeds evolved into tetrahedral Pt@Ru NCs after the growth of Ru shells, suggesting that {111} facets of *fcc* Ru were the most favored surfaces under the hydrothermal conditions. The DFT calculation showed that the surface formation energy of the (111) surface of *fcc* Ru (0.147 eV·Å^{-2}) was much lower than that of the (100) surface (0.188 eV·Å^{-2}), and water molecules can form compact honeycomb-type adsorption layer on the closest packed surface of Ru[27] which may further stabilize the (111) facets. Additionally, $C_2O_4^{2-}$ ions which specifically stabilize {111} facets of the *fcc* PtPd alloy in the synthesis of PtPd alloy tetrahedrons[28] might also stabilize {111} facets of *fcc* Ru. Ru shells in $Pt_{50}@Ru_{50}$ were not thick enough to construct a tetrahedron. Hence, most particles in this sample were octahedrons or truncated ones (Figures S1e and S3c).

If Na_2PdCl_4 was used instead of K_2PtCl_4 in the one-step synthesis, *fcc* Pd NCs with multitwinned structure and *hcp* Ru nanoplates were separately generated (Figure S6a, c). Since the reduction potential of $PdCl_4^{2-}$ (φ^θ = 0.591 V) was lower than that of $PtCl_4^{2-}$ (φ^θ = 0.73 V),[29] the generation of Pd^0 and Ru^0 monomers might be simultaneous, which was a probable reason why core−shell NCs were not synthesized. *hcp* Rh−Ru alloy nanoplates were obtained when $RhCl_3$ and $RuCl_3$ were coreduced through the one-step route, as revealed by EDS mapping and XRD refinement (Figure S6b, c). Lower

DOI: 10.1021/acs.jpcc.5b04587
J. Phys. Chem. C 2015, 119, 17697−17706

reduction potential of $RhCl_3$ (φ^θ = 0.431 V)[29] compared with the $PtCl_4^{2-}$ precursor would lead to the coreduction of Rh and Ru precursors. More importantly, based on DFT calculation, the energies to imbed an M atom (M = Pt, Pd, and Rh) into the *hcp* Ru lattice to form the M−Ru alloy were 0.297, 0.442, eV and −0.012 eV, respectively, indicating that the formation of the Rh−Ru alloy was thermodynamically more favored than that of Pt−Ru and Pd−Ru alloys, in agreement with the observations above.

If presynthesized *fcc* Pd and *fcc* Rh NCs (Figure S7) were used as seeds in the two-step method (the molar ratio of M:Ru (M = Pd, Rh) was 20:80 in the feedstock), Pd@Ru and Rh−Ru alloy NCs with the *fcc* structure were obtained, as validated by the EDS mapping images (Figures 4a,b and S7c-e) and XRD

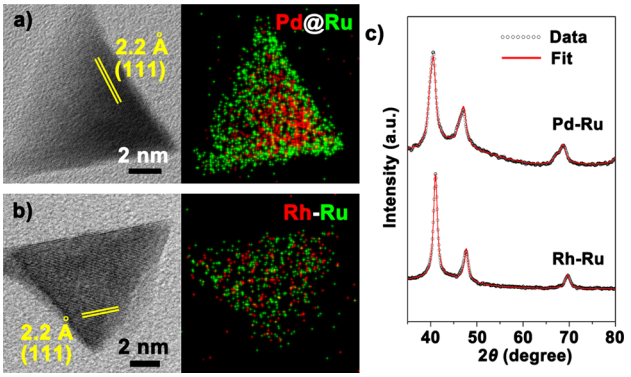

Figure 4. Characterizations of *fcc* Pd@Ru and *fcc* Rh−Ru alloy NCs synthesized with the two-step method. HRTEM and EDS mapping images of (a) a single crystalline Pd@Ru tetrahedron and (b) a single crystalline Rh−Ru alloy tetrahedron. Red regions represent Pd or Rh and green regions represent Ru. (c) XRD spectra (circles) and Rietveld refinement (red lines) of Pd@Ru and Rh−Ru alloy NCs. The fitting results were shown in Table S3.

spectra (Figure 4c). Since both single-crystalline and twinned NCs existed in the Pd and Rh seeds introduced for the deposition of Ru, the obtained bimetallic NCs adopted both kinds of structures (Figures 4 and S7). The molar ratios of M:Ru in the products were close to the loading ratios of two metals, as listed in Table S2, suggesting that both metals were reduced completely. It is noteworthy that, according to the Rietveld refinement results in Table S3, higher contribution of *hcp* Ru was observed in the XRD spectrum of Pd@Ru NCs compared with that of Pt@Ru NCs with the same Ru content, and in some Pd@Ru NCs the Ru shells were incomplete, leading to the exposure of the Pd surface, as shown in Figure S8d and confirmed by the Ag underpotential deposition (upd) test discussed later. These phenomena implied the interaction between Pd and Ru was weaker than that between Pt and Ru, which was verified by DFT calculation in the discussion later. More intriguingly, Rh and Ru formed *fcc* alloy NCs even when presynthesized Rh seeds were used, suggesting that the energy barrier for the interdiffusion between Rh and Ru in NCs was low enough for the formation of the alloy at 160 °C. The NCs kept the *fcc* structure during the gradual alloying process between *fcc* Rh seeds and newly deposited Ru atoms.

Some previous works have investigated the structure of Ru layers deposited on extended *fcc* metal substrates.[30−32] When polycrystalline Ru was deposited on the Pt surface, the Pt−Ru interface was unmatched and Ru still adopted the *hcp* phase.[30] When Ru films were epitaxially grown on the (111) facet, the closest packed facet, of Au or Pt, the Ru thin films retained the *hcp* phase with the closest packed surface, the (0001) facet, attached to the substrate.[31,32] To understand why these Ru films retained the *hcp* phase but Ru shells copied the *fcc* phase from the cores in our case, we compared the structures of the closest packed interface and nonclosest packed ones between Ru and *fcc* metals.

The difference between *fcc* and *hcp* structures is the stacking sequence of the closest packed atomic layers. The *fcc* phase adopts |ABC|ABC type stacking, while the *hcp* phase adopts |AC|AC type one. The transition among the closest packed layers 'A', "B', and 'C" can be realized by the lateral shift of the layers. Figure 5a shows the epitaxial Ru layers on the (111)

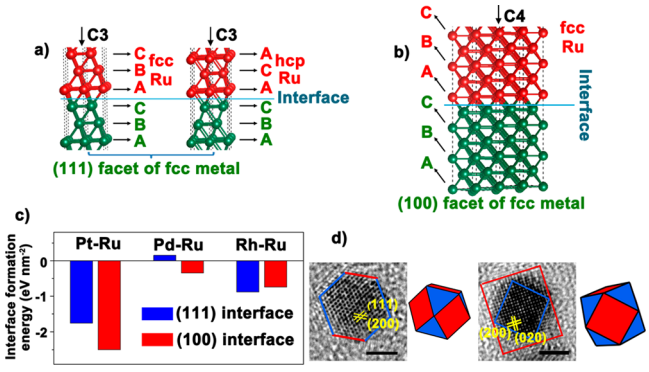

Figure 5. Analysis of the interface between Ru and *fcc* noble metals. (a) The structure of the interfaces between the (111) facet of the *fcc* metal and the (111) facet of *fcc* Ru (left) and the (0001) facet of *hcp* Ru (right). Both interfaces show C3 symmetry. (b) The structure of the interface between the (100) facet of the *fcc* metal and the (100) facet of *fcc* Ru from [011] zone-axis. This interface shows C4 symmetry. The closest packed layers were labeled as 'A', "B', and 'C" in panels (a) and (b). (c) DFT calculated formation energies of (111) and (100) interfaces between *fcc* Pt, Pd, Rh, and Ru. (d) HRTEM images and 3-D models of *fcc* Pt seeds with cubooctahedral morphology from (left) [01-1] and (right) [001] zone axes. Red and blue surfaces in these models represent {100} and {111} facets, respectively. The scale bars indicate 2 nm.

facet of the *fcc* metal. Since the closest packed layers are parallel to the interface, as indicated by the black arrows, the interface has no effect on the stacking type of the closest packed layers of Ru, namely both the *fcc* phase with |ABC|ABC type stacking or the *hcp* phase with |AC|AC type stacking can be adopted by the Ru layers. Under this circumstance, thermodynamically more favored the *hcp* phase of Ru[33] are more likely to form. However, when Ru atoms are epitaxially deposited on the (100) facet of the *fcc* metal, as shown in Figure 5b, the closest packed layers of Ru intersect with the interface. Supposing *hcp* Ru layers with |AC|AC type stacking form through the shift of the closest packed layers in the structure in Figure 5b, the interface will crack. Therefore, the *fcc* phase of Ru layers is "locked" on the (100) facet of the *fcc* metal. This conclusion can also be understood from the view of symmetry. Both the (111) facet of the *fcc* phase and the (0001) facet of the *hcp* phase show C3 symmetry, therefore *hcp* Ru layers match the (111) facet of the *fcc* metal. Whereas, the (100) facet of the *fcc* phase represents C4 symmetry but no facet of the *hcp* phase shows such symmetry, therefore *hcp* Ru cannot form the matched interface with the (100) facet of the *fcc* metal. Generally, except for the (111) facet, other facets of the *fcc*

DOI: 10.1021/acs.jpcc.5b04587
J. Phys. Chem. C 2015, 119, 17697−17706

metal could only form the perfectly matched interface with *fcc* Ru, such as the case on the (110) facet shown in Figure S9.

Based on the analyses above, when Ru shells were epitaxially grown on various facets of the *fcc* cores, especially the nonclosest-packed facets, they would follow the *fcc* structure of the cores. In this work, near-spherical *fcc* Pt NCs were used as seeds for the growth of Ru shells. Most of the Pt seeds adopted cubooctahedral morphology exposing both {111} and {100} facets, as illustrated by the HRTEM images and 3-D models in Figure 4d. During the formation of the Pt@Ru NCs, compact Ru shells formed all over the exposing facets of the Pt seeds, especially the considerable amount of nonclosest-packed facets. Hence, the Ru shells were guided into *fcc* structure. Moreover, according to DFT calculations, the (100) interfaces of Pt−Ru and Pd−Ru have lower formation energy than the (111) interfaces (Figure 5c), which may further facilitate the epitaxial growth of Ru layers on {100} facets of the seeds and the formation of *fcc* Ru shells. Additionally, the Pt−Ru interface was much more stable than the Pd−Ru interface, which was a probable reason why complete Ru shells were formed in Pt@Ru NCs while part of the Pd surface was uncovered in some Pd@Ru NCs (Figure S8d). A precise control of the reduction rate of $RuCl_3$ was essential to ensure the deposition of Ru^0 monomers on the surface of *fcc* seeds and, consequently, is indispensable for the formation of *fcc* Ru shells, especially on Pd cores. In our synthetic strategy, $Na_2C_2O_4$ ions were used to form complexes with Ru^{n+} ions[25,26] and HCl was added to lower the reducing capacity of HCHO.[34,35] Both reagents were aimed to slow down the reduction rate of Ru precursor.

The as-obtained bimetallic NCs can be well dispersed on carbon black (Vulcan XC-72R) by ultrasound treatment as electrocatalysts, as shown in Figure S10. All of the potentials given in this work were against reversible hydrogen electrode (RHE). Figure 6a compares the cyclic voltammetry (CV) curves of commercial Pt/C, hydrothermally synthesized Ru/C, and $Pt_{10}@Ru_{90}$/C in 0.1 M $HClO_4$ solution, in which the current densities were normalized to the electrochemical active surface area (ECSA) of the samples determined by Cu underpotential deposition (upd) stripping curves (Figure S11).[36] The broad peak in the cathodic scan of the CV curve of Pt/C at ~0.75 V corresponded to the reduction of adsorbed oxygen species on the Pt surface, while this process occurred on the Ru surface mainly at potential lower than 0.6 V, as marked in Figure 6a. Then, Ag underpotential deposition (upd) stripping voltammetry[37] can be used to determine the surface composition of the catalysts: The catalysts were first preoxidized at 1.1 V followed by the deposition of Ag atoms at 0.66 V. At this deposition potential, most Pt sites on the NCs were reduced, while Ru sites were still passivated by oxygen species. Therefore, Ag atoms were selectively deposited on Pt sites during this process. The deposited Ag atoms were stripped in an anodic sweep from the deposition potential, and the stripping current was an indication of Pt sites on the surface of NCs. As shown in Figure 6b-d and Figure S12, the stripping current was detected on commercial Pt/C and commercial PtRu alloy/C and was negligible on Ru/C and Pt@Ru NCs/C, validating that the surface of Pt@Ru NCs was dominated by Ru sites. Therefore, the electrocatalytic activity of Pt@Ru NCs discussed later purely came from the Ru sites on the surface of *fcc* Ru shells. Additionally, considerable stripping current was observed on Pd@Ru NCs/C (Figure S12), indicating part of the Pd core surface was not covered by Ru shells. Rh−Ru alloy NCs/C did not show obvious stripping current because the Rh

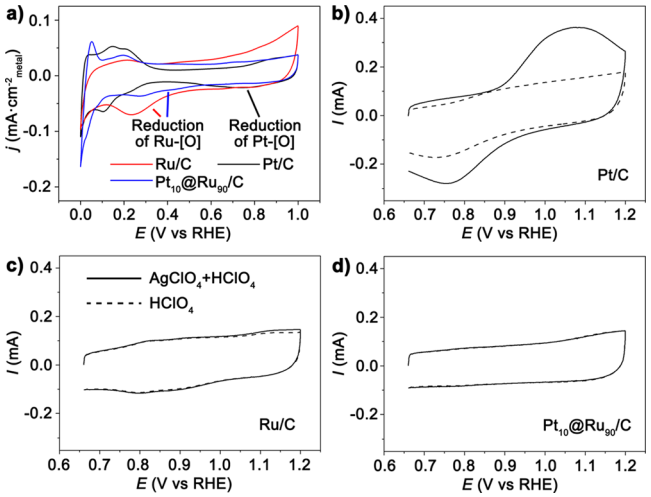

Figure 6. (a) CV curves of commercial Pt/C (black), hydrothermally synthesized Ru/C (red), and $Pt_{10}@Ru_{90}$/C (blue) in N_2 saturated 0.1 M $HClO_4$ solution. The scan rate was 50 mV s^{-1}. The current density was normalized to the ECSA of the catalysts deduced from the Cu upd stripping curves. (b-d) Ag upd stripping curves of (b) commercial Pt/C, (c) hydrothermally synthesized Ru/C and (d) $Pt_{10}@Ru_{90}$/C. The catalysts were first preoxidized at 1.1 V in 0.1 M $HClO_4$ solution for 100 s and then kept at 0.66 V in 1 mM $AgClO_4$ + 0.1 M $HClO_4$ solution (solid curves) or 0.1 M $HClO_4$ solution (dashed curves) for another 100 s, followed by a cycle of voltammatric sweep between 0.66 and 1.2 V with the scan rate of 50 mV s^{-1}. The difference between solid and dashed curves in the anodic sweeps is the stripping current of upd Ag.

sites were also passivated by oxygen species at the deposition potential.[38]

Figure 7a shows the HOR polarization curves obtained on *fcc* Pt@Ru NCs/C (solid curves), hydrothermally synthesized Ru/C (as-prepared, black dashed curves), and commercial Pt/C (gray dashed curves) loaded on glassy carbon rotating disk electrode (RDE) with the rotation speed of 2500 rpm in H_2 saturated 0.1 M $HClO_4$ solution. Figure S13 shows the Koutecky−Levich plot of HOR on $Pt_{10}@Ru_{90}$/C, and the exchange electron number (n) of HOR was determined to be 1.9, which was quite close to two. The kinetic currents (I_k) of HOR for all samples were also deduced from Koutecky−Levich analysis. Figures 7b and 7c show the curves of the kinetic current densities normalized to the total mass of Pt and Ru (j_m) and to the ECSA (Figure 7d) deduced from Cu upd stripping curves (j_A), respectively, in the linear-current potential region near 0 V, and the exchange current densities (j_0) were calculated from these curves by using the approximate Butler−Volmer equation[38,39]

$$j_k = j_0(n\eta F/RT) \quad (1)$$

where the exchange electron number (n) equals two, η is the overpotential, and R and F have the conventional meaning. The fitting results reflected the mass activity and specific activity respectively, as shown in Figures 7e and 7f. Significantly higher HOR activity was achieved on *fcc* Pt@Ru NCs/C than on Ru/C, and $Pt_{10}@Ru_{90}$/C showed the highest activity among the core−shell samples, i.e. 0.19 A·mg^{-1} and 0.30 mA·cm^{-2}. These values are more than an order of magnitude higher than those on as-prepared Ru/C (0.016 A·mg^{-1} and 0.017 mA·cm^{-2}) and comparable with those of commercial Pt/C (0.23 A·mg^{-1} and 0.27 mA·cm^{-2}). Figure S14 shows the TEM image of Pt_{10}@

DOI: 10.1021/acs.jpcc.5b04587
J. Phys. Chem. C 2015, 119, 17697−17706

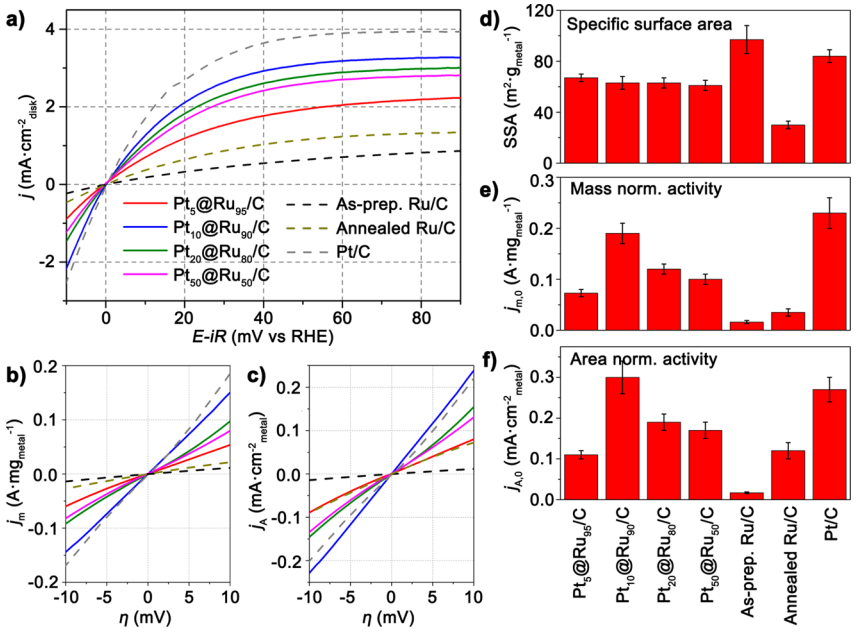

Figure 7. (a) HOR polarization curves with *iR*-compensation obtained on Pt@Ru NCs/C (solid lines), as-prepared Ru/C (black dashed line), 500 °C annealed Ru/C (brown dashed line), and commercial Pt/C (gray dashed line) in 0.1 M $HClO_4$ aqueous solution saturated with H_2. Sweep rate: 5 mV s^{-1}; rotation speed: 2500 rpm; temperature: 25 °C; loading of total metal mass: 3 μg. Curves of the kinetic current densities of all samples normalized to (b) total metal mass and (c) ECSA depending on overpotential in the linear-current potential region near 0 V. (d) Specific surface area (SSA) deduced from Cu upd stripping curves and ICP-AES and (e) mass-normalized and (f) ECSA-normalized exchange current densities of all samples.

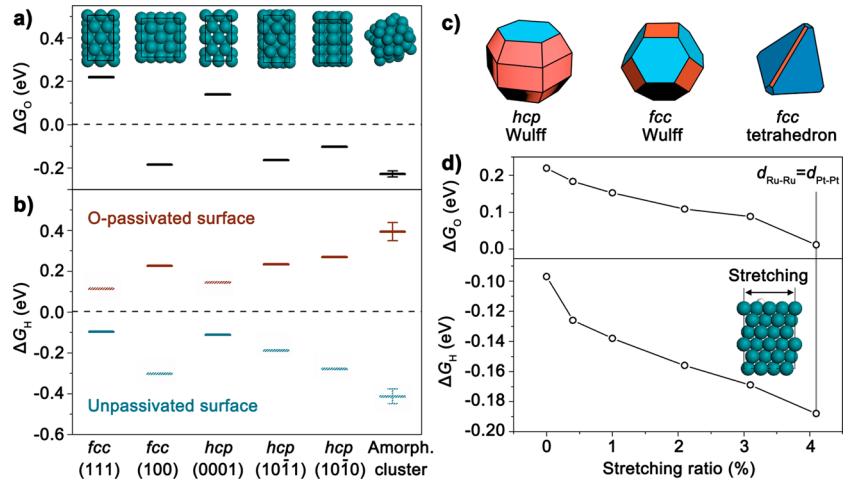

Figure 8. (a) The free energy to form adsorbed oxygen at 0 V vs RHE (ΔG_O) and (b) the dissociated adsorption energy of hydrogen (ΔG_H) on the bare surfaces (blue) and oxygen-passivated surfaces (brown) of *fcc* and *hcp* Ru slabs and amorphous Ru clusters. The insets of panel (a) show the top-views of the supercells of Ru slabs and a Ru_{50} amorphous cluster used in the DFT calculations. The coverage of oxygen on slabs involved in this figure was 50%. (c) Wulff polyhedrons of the *hcp* phase (left) and the *fcc* phase (middle) and an *fcc*-phase tetrahedron. Blue regions are the closest packed surface and brown regions are the open surface. (d) Plots of ΔG_O (upper) and ΔG_H (lower) on the bare (111) slab of *fcc* Ru depending on the lateral stretching ratio. The gray vertical line indicates the situation that the lattice parameter of the slab equals that of *fcc* Pt.

Ru_{90}/C after the electrochemical test, in which the NCs still maintained the tetrahedral morphology, indicating the catalyst was stable during the HOR test. The catalytic performances of Pd@Ru NCs/C and Rh−Ru alloy NCs/C toward HOR were also tested, as shown in Figure S15. However, since both Ru sites and Pd (or Rh) sites could be the origin of HOR activity[40,41] of these samples, it is difficult to extract the contribution of Ru sites to the overall activity.

The Ru NSs after hydrothermal synthesis were poorly crystallized particles with the average size of 3.8 nm, as shown in Figure S16a-c. To investigate whether crystallinity or phase is the key factor determining the HOR activity of Ru nanocatalysts, we prepared well crystallized Ru/C by annealing the as-prepared Ru/C in N_2 at 500 °C for 5 h. The obtained catalyst aggregated significantly and clearly shows the *hcp* structure (Figure S16d-g). Enhanced specific activity (0.12 mA·cm^{-2} as shown in Figure 7f) was achieved on the annealed Ru/C, but this value was still much lower than that of Pt_{10}@Ru_{90}/C, indicating that well crystallized Ru catalysts showed higher HOR activity than poorly crystallized ones and *fcc* Ru catalysts enclosed by {111} facets were more active than the *hcp* Ru catalysts.

DOI: 10.1021/acs.jpcc.5b04587
J. Phys. Chem. C 2015, 119, 17697−17706

Some previous works have shown that the adsorption of oxygen species strongly suppresses the HOR activity of *hcp* Ru catalysts,[22] and the crystallinity and surface oxidation level of Ru nanocatalysts have a great effect on their HOR activity in the alkaline electrolyte.[19] XPS analyses of Ru-3p electrons (Figure S17) indicated that the as-prepared Ru NSs showed a higher surface oxidation level than the Pt@Ru NCs also synthesized with the hydrothermal method, and among the CV curves collected in N_2 saturated 0.1 M $HClO_4$ solution (Figure 6a and Figure S18), the as-prepared Ru/C showed much higher oxidation current density in the anodic scan from 0.4 to 1.0 V compared with other well crystallized samples. These results suggested that the surface of the poorly crystallized Ru/C catalyst was more likely to be deeply oxidized in air or at high potential under electrochemical conditions, and the well crystallized catalysts were comparatively more inert to oxidation. However, what is the relationship between the surface oxidation level and the catalytic activity and how the crystallinity and the phase of the catalysts affect these properties are still open questions.

DFT calculations were then used to help us to understand the structure−activity correlations. We calculated the free energy for oxygen adsorption at 0 V vs RHE (ΔG_O, corresponding to $* + H_2O \rightarrow O^* + 2H^+ + 2e^-$) and the dissociated adsorption free energy of a hydrogen atom on the surface (ΔG_H, corresponding to $* + 1/2H_2 \rightarrow H^*$) with and without the adsorption of oxygen on different slabs of *hcp* and *fcc* Ru and amorphous Ru_{50} clusters. Ru_{50} amorphous clusters were constructed by *ab initio* molecular dynamics (MD) at 3000 K followed by ionic relaxations with the conjugate gradient (CG) method, and the average data on five different clusters were finally used. We were only concerned with the situation on Ru slabs adsorbed half-coverage oxygen adatoms, since the free energies to form full-coverage oxygen layers are calculated to be positive at 0 V on all Ru slabs (Table S4). The (0001) facet of *hcp* Ru and the (111) facet of *fcc* Ru showed positive ΔG_O, as shown in Figure 8a and Table S5, indicating that these surfaces are comparably inert at 0 V. On the contrary, due to the existence of the undercoordinated sites, the open surfaces of Ru slabs and amorphous Ru clusters showed negative ΔG_O, indicating these surfaces tended to be partially passivated by oxygen at 0 V. Similarly, the adsorption of hydrogen was stronger on these surfaces, especially on amorphous Ru clusters, than on the closest packed surface, as shown in the lower part of Figure 8b and Table S6. The (111) facet of *fcc* Ru adsorbed hydrogen a little weaker than the (0001) facet of *hcp* Ru, probably because the lateral interatomic distance in the (111) facet of *fcc* Ru (2.70 Å) is slightly smaller than that in the (0001) facet of *hcp* Ru (2.72 Å). Oxygen and hydrogen atoms preferentially occupied the same kind of sites on a given surface, such as the triple sites on the (10−11) surface and the bridge sites on the (10−10) surface (Figures S20 and S21). When oxygen atoms were adsorbed on the surfaces, ΔG_H increased from negative to positive on all the surfaces (upper part of Figure 8b and Table S7), since the surfaces became crowded for hydrogen adsorption. More importantly, opposite to the situation on bare Ru surfaces, ΔG_H on open surfaces became higher than that on the closest packed surfaces, because the available sites for hydrogen adsorption on open surfaces were no longer the preferential adsorption sites on the bare surfaces.

A highly active HOR catalyst should balance the chemisorption of hydrogen and oxidation-desorption of adsorbed hydrogen atom and, hence, show ΔG_H close to zero.[23,42,43] When amorphous Ru clusters were used as HOR catalysts, the surface was passivated by oxygen, and the value of ΔG_H of this surface was much higher than 0. The values of ΔG_H of all *hcp* and *fcc* slabs were closer to 0 than that of amorphous clusters. We also calculated the values of ΔG_H on *fcc* Ru_{56} tetrahedrons enclosed by {111} facets and *hcp* Ru_{69} trigonal bipyramid enclosed by {10−11} facets which adopted the same adsorption configuration of the (111) slab of *fcc* Ru and the (10−11) slab of *hcp* Ru, respectively (Figure S22). The adsorption of hydrogen on these clusters was only slightly stronger than that on the corresponding slab models (Table S8), suggesting that the difference between the values of ΔG_H on the amorphous Ru_{50} clusters and on the Ru slabs mainly resulted from different crystallinity. Therefore, well crystallized Ru catalysts should exhibit higher HOR activity than amorphous or poorly crystallized Ru catalysts. On the other hand, the values of ΔG_H on the closest packed facets were closer to 0 than those on the open surfaces, no matter if the surfaces were partially covered by oxygen or not. Since the *fcc* structure shows higher symmetry than the *hcp* phase, more of the closest packed surface are possible to be exposed on *fcc* particles, as illustrated by the Wulff polyhedrons in Figure 8c. Moreover, *fcc* Pt@Ru tetrahedrons maximize the exposure of {111} facets. Therefore, it is comprehensible that *fcc* Pt@Ru tetrahedrons/C exhibited higher HOR activity than *hcp* Ru/C catalysts.

According to the XRD refinement, 18 wt % of poorly crystallized Ru particles existed in $Pt_5@Ru_{95}$, which might depress the overall HOR activity of this sample. Moreover, the existence of Pt cores led to the lattice extension of the *fcc* Ru shells and as the Pt content increased the extension increased, which also affected the adsorption behaviors and the HOR activity. The d-band of surface Ru atoms became narrow and rose as the lattice expanded,[44,45] leading to stronger adsorption of hydrogen and oxygen, as shown by Figure 8d and Table S9. ΔG_O of (111) slab of *fcc* Ru was still positive as the lattice parameter increased to that of *fcc* Pt, suggesting that the surface of *fcc* Pt@Ru tetrahedrons was not passivated by oxygen. The lattice expansion led to more negative ΔG_H value which was detrimental to HOR. Therefore, HOR activity *fcc* Pt@Ru tetrahedrons/C decreased as the Pt content increased and $Pt_{10}@Ru_{90}$/C exhibited the highest HOR activity.

CONCLUSION

A new phase control strategy was developed to prepare *fcc* Ru nanocatalysts, in which Ru shells were epitaxially grown on the surfaces of *fcc* Pt and Pd seeds and the seeds guided the Ru shells inheriting the *fcc* structure. Specifically, monodisperse *fcc* Pt@Ru tetrahedrons enclosed by {111} facets were prepared with a one-step hydrothermal method. The theoretical analysis of bimetallic interface structures showed that the epitaxial growth of Ru layers on diverse facets of the *fcc* metal seeds, especially on the nonclosest-packed facets, led to the formation of *fcc* Ru shells. Moreover, *fcc* Pt@Ru tetrahedrons/C exhibited greatly enhanced electrocatalytic activity toward HOR compared with Ru/C catalysts. Electrochemical measurements combined with DFT calculations revealed that the high crystallinity and the maximum exposure of {111} facets of *fcc* Ru imparted *fcc* Pt@Ru tetrahedrons/C HOR activity enhancement. This work provided a facile method to prepare well crystallized *fcc* Ru nanocatalysts with uniform morphology and achieved the optimized catalytic activity through the phase and

DOI: 10.1021/acs.jpcc.5b04587
J. Phys. Chem. C 2015, 119, 17697−17706

morphology control. This method is promising to prepare more nanomaterials with metastable phases and investigate the phase, shape, and size effects on their catalytic performances.

METHODS

Chemicals. K_2PtCl_4, $RuCl_3{\cdot}xH_2O$, $RhCl_3$, $PdCl_2$ (all the noble metal precursors were in A.R. grade and purchased from Shengyang Institute of Nonferrous Metal), sodium oxalate ($Na_2C_2O_4$, A.R.), poly(vinylpyrrolidone) (PVP; Mw ~ 29,000, Sigma-Aldrich), formaldehyde aqueous solution (HCHO, 40%, A.R.), hydrochloride acid (HCl, A.R.), acetone (A.R.), carbon black (Vulcan XC-72R, Cabot), the Pt/C catalyst (20 wt % Pt, Shanghai Hesen Electric Co. Ltd.), PtRu alloy/C (30 wt %, Shanghai Hesen Electric Co. Ltd.), perchloric acid ($HClO_4$, A.R.), ethanol (A.R.), and Nafion (5% ethanol solution, Alfa Aesar) were used as received. Na_2PdCl_4 solution was prepared by mixing and dissolving $PdCl_2$ and NaCl with water at room temperature under stirring overnight. $AgClO_4$ and $Cu(ClO_4)_2$ solution was prepared by dissolving Ag_2O (A.R.) and CuO (A.R.) with $HClO_4$ solution, respectively. Ultrapure N_2 and H_2 were used in the electrochemical tests. The water used in all experiments was ultrapure (Millipore, 18.2 MΩ cm).

Hydrothermal Synthesis of Nanocrystals. The hydrothermal synthesis was carried out in 25 mL Teflon-lined containers sealed in stainless steel autoclaves. In the one-step synthesis of Pt@Ru NCs, K_2PtCl_4 and $RuCl_3{\cdot}xH_2O$ (the total amount of the Pt and Ru precorsors was 0.24 mmol), 100 mg of PVP, 80 mg of $Na_2C_2O_4$, 0.1 mL of HCHO solution, and 0.062 mL of 1 M HCl solution were dissolved in ultrapure water, diluted to 15 mL, loaded into the container, and sealed in the autoclave. The autoclave was then transferred into an oven kept at 160 °C and taken out after 8 h. After the reaction solution was cooled to room temperature, the crude product was purified by dialysis for 2 days in ultrapure water. The NCs were subsequently collected by adding acetone and centrifugation and washed by water−acetone (v/v = 1:3) mixed solution for 3 times. Vacuum dried black powders were used for XRD and XPS characterizations, and the sample dispersed in 5 mL of ethanol was used for TEM and electrochemical characterizations.

In the two-step synthesis of Pt@Ru NCs, Pt seeds were first synthesized with the hydrothermal method. The recipe of the reaction solution was the same as that in the one-step synthesis, except that only 0.048 mmol of K_2PtCl_4 was used as the metal precursor. The reaction was kept at 160 °C for 4 h, and the Pt seeds were collected by adding acetone and centrifugation. The as-synthesized Pt seeds were then added into the reaction solution for the second step which was the same as that in the one-step synthesis, except that only 0.192 mmol of $RuCl_3{\cdot}xH_2O$ was used as the metal precursor. The reaction was kept at 160 °C for 8 h, followed by the same post-treatment procedures used in the one-step synthesis.

The strategy of the two-step synthesis of Pd@Ru and Rh−Ru alloy NCs was the same as that of the two-step synthesis of Pt@Ru NCs, except that the same amount of Na_2PdCl_4 or $RhCl_3$ was used instead of K_2PtCl_4.

Ru nanospheres were synthesized with the hydrothermal method according to the previous work[26] as shown in the Supporting Information (SI).

Characterization. The sample for TEM characterization was prepared by drying a drop of ethanol dispersion of the NCs on an ultrathin carbon film supported by a copper grid. TEM and HRTEM images were taken on an FEI Tecnai F30 operated at 300 kV. HAADF-STEM and EDS mapping images were obtained from an FEI TITAN Cs-corrected ChemiSTEM operated at 200 kV, which incorporated a probe corrector and a super-X EDS system. XRD spectra were collected on an X pert pro diffractometer (Philips, Netherland) using Cu Kα radiation with a scan speed of 2° min^{-1}. The contribution of Kα2 line was subtracted. ICP-AES analysis was used to quantify the mass of metal in NCs and was conducted on a Profile Spec ICP-AES spectrometer (Leeman, U.S.). The XPS spectra were obtained from an Axis Ultra (Kratos, Japan) imaging photoelectron spectrometer.

Electrochemical Tests. Carbon black (Vulcan XC-72R) with 4 times the mass of metal was added to the ethanol dispersion (5 mL) of the metal NCs, followed by the addition of 5 drops of cyclohexane, and the mixture was treated with ultrasound for 5 h to deposite the NCs on carbon black. The supported NCs were then collected by centrifugation and redispersed in ethanol solution containing 0.2% Nafion to form ink with 1 mg mL^{-1} of NCs/C, and the ink was treated with ultrasound for 30 min to form a homogeneous suspension. The content of metal in this ink was then analyzed by ICP-AES. A PGSTAT302N (Autolab Corp., Switzerland) electrochemical analyzer with an impedance module was used for the electrochemical measurements, combined with a glassy carbon rotating disk electrode (RDE, 5 mm in diameter) setup (Pine, U.S.) as a work electrode, a saturated Ag/AgCl reference electrode, and a Pt foil as counter electrode. The potentials given in this work were against RHE. The as-prepared ink containing 3 μg of metal was dropped on the RDE and dried, followed by UV-ozone treatment by illuminating the RDE with a UV lamp (10 W, with 185 and 254 nm emissions) at the distance of ~5 mm for 5 h and rinsing the RDE with ultrapure water.[46] All the electrochemical measurements were carried out at 25 °C. 40 cycles of CV sweep between 0.0 and 1.0 V in N_2 saturated 0.1 M $HClO_4$ solution was first carried out to obtain stable CV curves. Then the HOR test, the Cu upd stripping test, and the Ag upd stripping test were carried out in sequence. To correct the *iR*-drop in the HOR tests, impedance measurements at 0.1 V with the potential amplitude of 10 mV were applied with frequencies from 100 kHz to 1 Hz on a logarithmic scale.[47] All the electrochemical properties reported in this paper were obtained from three independent measurements, which showed good repeatability.

DFT Calculation Methods. All DFT calculations were performed by using projected augmented wave (PAW) potentials[48] and the Perdew−Burke−Ernzerhof (PBE) functional[49] implemented in the Vienna ab initio simulation package (VASP).[50] The cutoff energy was set at 400 eV for relaxation and *ab initio* MD and 500 eV for the computation of single point energy. Monkhorst−Pack k-points sampling with the density of k-points higher than 0.03 $Å^{-1}$ was used in all calculations. The DFT-optimized lattice constants, a = 3.82 Å for *fcc* Ru and a = 2.72 Å and c = 4.31 Å for *hcp* Ru, were used to build up the slabs and clusters. In the calculation of ΔG_H and ΔG_O, each supercell of the slab model contained 6 layers of Ru atoms and 15 Å of vacuum layer, and the top three layers of Ru atoms and the adsorbed atoms were allowed to move in the relaxation steps with the CG method, followed by the calculation of single point energy and zero point energy. By comparing the single point energies of different adsorption configurations, we determined the adsorption sites for hydrogen and oxygen atoms, in agreement with some previous reports.[51−53] Ru clusters and molecules were put in cubic boxes

DOI: 10.1021/acs.jpcc.5b04587
J. Phys. Chem. C 2015, 119, 17697−17706

with the size of 30 Å in the calculations. Amorphous Ru clusters were constructed by *ab initio* MD at 3000 K followed by ionic relaxations with the CG method. More calculation details are in the Computation Section of the Supporting Information, including calculation results (Tables S4–S9) and the structure of supercells (Figures S19–S22).

■ ASSOCIATED CONTENT

Supporting Information

The Supporting Information is available free of charge on the ACS Publications website at DOI: 10.1021/acs.jpcc.5b04587.

Synthesis method of Ru NSs, more TEM, XRD, electrochemical characterization results, and DFT calculation details (PDF)

■ AUTHOR INFORMATION

Corresponding Authors

*E-mail: ywzhang@pku.edu.cn (Y.-W.Z.).
*E-mail: wxli@dicp.ac.cn (W.-X.L.).

Notes

The authors declare no competing financial interest.

■ ACKNOWLEDGMENTS

This work was supported by the NSFC (21025101, 21271011, 51222202, 51472215, 21225315, and 21321001), the National Basic Research Program of China (2014CB932500, 2013CB834603), the Program for Innovative Research Team in University of Ministry of Education of China (IRT13037), and the Fundamental Research Funds for the Central Universities (2014XZZX003-07 and 2015CB92100). Y.W.Z. particularly appreciates the financial aid of China National Funds for Distinguished Young Scientists from the NSFC. We also thank Prof. De-Chun Zou and Mr. Ming Peng for the help with electrochemical characterization.

■ REFERENCES

(1) Kusada, K.; Kobayashi, H.; Yamamoto, T.; Matsumura, S.; Sumi, N.; Sato, K.; Nagaoka, K.; Kubota, Y.; Kitagawa, H. Discovery of Face-Centered-Cubic Ruthenium Nanoparticles: Facile Size-Controlled Synthesis Using the Chemical Reduction Method. *J. Am. Chem. Soc.* **2013**, *135*, 5493−5496.

(2) Joo, S. H.; Park, J. Y.; Renzas, J. R.; Butcher, D. R.; Huang, W.; Somorjai, G. A. Size Effect of Ruthenium Nanoparticles in Catalytic Carbon Monoxide Oxidation. *Nano Lett.* **2010**, *10*, 2709−2713.

(3) Braconnier, L.; Landrivon, E.; Clémençon, I.; Legens, C.; Diehl, F.; Schuurman, Y. How Does Activation Affect the Cobalt Crystallographic Structure? An *in situ* XRD and Magnetic Study. *Catal. Today* **2013**, *215*, 18−23.

(4) Gnanamani, M. K.; Jacobs, G.; Shafer, W. D.; Davis, B. H. Fischer−Tropsch Synthesis: Activity of Metallic Phases of Cobalt Supported on Silica. *Catal. Today* **2013**, *215*, 13−17.

(5) Liu, J.-X.; Su, H.-Y.; Sun, D.-P.; Zhang, B.-Y.; Li, W.-X. Crystallographic Dependence of CO Activation on Cobalt Catalysts: HCP versus FCC. *J. Am. Chem. Soc.* **2013**, *135*, 16284−16287.

(6) Kitakami, O.; Sato, H.; Shimada, Y.; Sato, F.; Tanaka, M. Size Effect on the Crystal Phase of Cobalt Fine Particles. *Phys. Rev. B: Condens. Matter Mater. Phys.* **1997**, *56*, 13849−13854.

(7) Dassenoy, F.; Casanove, M. J.; Lecante, P.; Pan, C.; Philippot, K.; Amiens, C.; Chaudret, B. Size and Composition Effects in Polymer-Protected Ultrafine Bimetallic Pt_xRu_{1-x} ($0 < x < 1$) Particles. *Phys. Rev. B: Condens. Matter Mater. Phys.* **2001**, *63*, 235407.

(8) Hills, C. W.; Mack, N. H.; Nuzzo, R. G. The Size-Dependent Structural Phase Behaviors of Supported Bimetallic (Pt-Ru) Nanoparticles. *J. Phys. Chem. B* **2003**, *107*, 2626−2636.

(9) Tian, W.; Sun, H. P.; Pan, X. Q.; Yu, J. H.; Yeadon, M.; Boothroyd, C. B.; Feng, Y. P.; Lukaszew, R. A.; Clarke, R. Hexagonal Close-Packed Ni Nanostructures Grown on the (001) Surface of MgO. *Appl. Phys. Lett.* **2005**, *86*, 131915.

(10) Schaefer, Z. L.; Weeber, K. M.; Misra, R.; Schiffer, P.; Schaak, R. E. Bridging hcp-Ni and Ni3C via a Ni3C1-x Solid Solution: Tunable Composition and Magnetism in Colloidal Nickel Carbide Nanoparticles. *Chem. Mater.* **2011**, *23*, 2475−2480.

(11) Alayoglu, S.; Nilekar, A. U.; Mavrikakis, M.; Eichhorn, B. Ru-Pt Core-Shell Nanoparticles for Preferential Oxidation of Carbon Monoxide in Hydrogen. *Nat. Mater.* **2008**, *7*, 333−338.

(12) Alayoglu, S.; Zavalij, P.; Eichhorn, B.; Wang, Q.; Frenkel, A. I.; Chupas, P. Structural and Architectural Evaluation of Bimetallic Nanoparticles: A Case Study of Pt−Ru Core−Shell and Alloy Nanoparticles. *ACS Nano* **2009**, *3*, 3127−3137.

(13) Chou, H.-l.; Lai, F.-J.; Su, W.-N.; Pillai, K. C.; Sarma, L. S.; Hwang, B.-J. Investigation of Formation Mechanism of Pt(111) Nanoparticle Layers Grown on Ru(0001) Core. *Langmuir* **2011**, *27*, 1131−1135.

(14) Hsieh, Y. C.; Zhang, Y.; Su, D.; Volkov, V.; Si, R.; Wu, L. J.; Zhu, Y. M.; An, W.; Liu, P.; He, P.; Ye, S. Y.; Adzic, R. R.; Wang, J. X. Ordered Bilayer Ruthenium-Platinum Core-Shell Nanoparticles as Carbon Monoxide-Tolerant Fuel Cell Catalysts. *Nat. Commun.* **2013**, *4*, 2466.

(15) Gu, J.; Liu, W.-C.; Zhao, Z.-Q.; Lan, G.-X.; Zhu, W.; Zhang, Y.-W. Pt/Ru/C Nanocomposites for Methanol Electrooxidation: How Ru Nanocrystals' Surface Structure Affects Catalytic Performance of Deposited Pt Particles. *Inorg. Chem. Front.* **2014**, *1*, 109−117.

(16) Fan, Z.; Zhu, Y.; Huang, X.; Han, Y.; Wang, Q.; Liu, Q.; Huang, Y.; Gan, C. L.; Zhang, H. Synthesis of Ultrathin Face-Centered-Cubic Au@Pt and Au@Pd Core−Shell Nanoplates from Hexagonal-Close-Packed Au Square Sheets. *Angew. Chem., Int. Ed.* **2015**, *54*, 5672−5676.

(17) Watt, J.; Yu, C.; Chang, S. L. Y.; Cheong, S.; Tilley, R. D. Shape Control from Thermodynamic Growth Conditions: The Case of hcp Ruthenium Hourglass Nanocrystals. *J. Am. Chem. Soc.* **2013**, *135*, 606−609.

(18) Velazquez, A.; Centellas, F.; Garrido, J. A.; Arias, C.; Rodriguez, R. M.; Brillas, E.; Cabot, P. L. Structure of Carbon-Supported Pt-Ru Nanoparticles and Their Electrocatalytic Behavior for Hydrogen Oxidation Reaction. *J. Power Sources* **2010**, *195*, 710−719.

(19) Ohyama, J.; Sato, T.; Yamamoto, Y.; Arai, S.; Satsuma, A. Size Specifically High Activity of Ru Nanoparticles for Hydrogen Oxidation Reaction in Alkaline Electrolyte. *J. Am. Chem. Soc.* **2013**, *135*, 8016−8021.

(20) Strmcnik, D.; Uchimura, M.; Wang, C.; Subbaraman, R.; Danilovic, N.; van der Vliet, D.; Paulikas, A. P.; Stamenkovic, V. R.; Markovic, N. M. Improving the Hydrogen Oxidation Reaction Rate by Promotion of Hydroxyl Adsorption. *Nat. Chem.* **2013**, *5*, 300−306.

(21) Montero, M. A.; Fernandez, J. L.; de Chialvo, M. R. G.; Chialvo, A. C. Kinetic Study of the Hydrogen Oxidation Reaction on Nanostructured Iridium Electrodes in Acid Solutions. *J. Phys. Chem. C* **2013**, *117*, 25269−25275.

(22) Inoue, H.; Wang, J. X.; Sasaki, K.; Adzic, R. R. Electrocatalysis of H_2 Oxidation on Ru(0001) and Ru(10−10) Single Crystal Surfaces. *J. Electroanal. Chem.* **2003**, *554-555*, 77−85.

(23) Nørskov, J. K.; Bligaard, T.; Logadottir, A.; Kitchin, J. R.; Chen, J. G.; Pandelov, S.; Stimming, U. Trends in the Exchange Current for Hydrogen Evolution. *J. Electrochem. Soc.* **2005**, *152*, J23−J26.

(24) Haglund, J.; Guillermet, A. F.; Grimvall, G.; Korling, M. Theory of Bonding in Transition-Metal Carbides and Nitrides. *Phys. Rev. B: Condens. Matter Mater. Phys.* **1993**, *48*, 11685−11691.

(25) Hoshino, Y.; Eto, M.; Fujino, T.; Yukawa, Y.; Ohta, T.; Endo, A.; Shimizu, K.; Sato, G. P. Synthesis and Characterization of Mixed-Ligand Ruthenium(III) Complexes with Oxalate and Acetylacetonate Ions. *Inorg. Chim. Acta* **2004**, *357*, 600−604.

(26) Yin, A.-X.; Liu, W.-C.; Ke, J.; Zhu, W.; Gu, J.; Zhang, Y.-W.; Yan, C.-H. Ru Nanocrystals with Shape-Dependent Surface-Enhanced Raman Spectra and Catalytic Properties: Controlled Synthesis and DFT Calculations. *J. Am. Chem. Soc.* **2012**, *134*, 20479−20489.

DOI: 10.1021/acs.jpcc.5b04587
J. Phys. Chem. C 2015, 119, 17697−17706

(27) Michaelides, A.; Alavi, A.; King, D. A. Different Surface Chemistries of Water on Ru{0001}: From Monomer Adsorption to Partially Dissociated Bilayers. *J. Am. Chem. Soc.* **2003**, *125*, 2746−2755.
(28) Yin, A.-X.; Min, X.-Q.; Zhang, Y.-W.; Yan, C.-H. Shape-Selective Synthesis and Facet-Dependent Enhanced Electrocatalytic Activity and Durability of Monodisperse Sub-10 nm Pt−Pd Tetrahedrons and Cubes. *J. Am. Chem. Soc.* **2011**, *133*, 3816−3819.
(29) Bratsch, S. G. Standard Electrode-Potentials and Temperature Coefficients in Water at 298.15 K. *J. Phys. Chem. Ref. Data* **1989**, *18*, 1−21.
(30) Liu, F.; Lee, J. Y.; Zhou, W. J. Multisegment PtRu Nanorods: Electrocatalysts with Adjustable Bimetallic Pair Sites. *Adv. Funct. Mater.* **2005**, *15*, 1459−1464.
(31) Kim, S. K.; Han, J. H.; Kim, G. H.; Hwang, C. S. Investigation on the Growth Initiation of Ru Thin Films by Atomic Layer Deposition. *Chem. Mater.* **2010**, *22*, 2850−2856.
(32) Kim, S. K.; Han, S.; Kim, G. H.; Jang, J. H.; Han, J. H.; Hwang, C. S. Local Epitaxial Growth of Ru Thin Films by Atomic Layer Deposition at Low Temperature. *J. Electrochem. Soc.* **2011**, *158*, D477−D481.
(33) Cohen, R. E.; Mehl, M. J.; Papaconstantopoulos, D. A. Tight-Binding Total-Energy Method for Transition and Noble-Metals. *Phys. Rev. B: Condens. Matter Mater. Phys.* **1994**, *50*, 14694−14697.
(34) Yin, A.-X.; Min, X.-Q.; Zhu, W.; Wu, H.-S.; Zhang, Y.-W.; Yan, C.-H. Multiply Twinned Pt-Pd Nanoicosahedrons as Highly Active Electrocatalysts for Methanol Oxidation. *Chem. Commun.* **2012**, *48*, 543−545.
(35) Gu, J.; Zhang, Y.-W.; Tao, F. Shape Control of Bimetallic Nanocatalysts through Well-Designed Colloidal Chemistry Approaches. *Chem. Soc. Rev.* **2012**, *41*, 8050−8065.
(36) Green, C. L.; Kucernak, A. Determination of the Platinum and Ruthenium Surface Areas in Platinum−Ruthenium Alloy Electrocatalysts by Underpotential Deposition of Copper. I. Unsupported Catalysts. *J. Phys. Chem. B* **2002**, *106*, 1036−1047.
(37) Herrero, E.; Buller, L. J.; Abruña, H. D. Underpotential Deposition at Single Crystal Surfaces of Au, Pt, Ag and Other Materials. *Chem. Rev.* **2001**, *101*, 1897−1930.
(38) Yuan, Q.; Zhou, Z.; Zhuang, J.; Wang, X. Seed Displacement, Epitaxial Synthesis of Rh/Pt Bimetallic Ultrathin Nanowires for Highly Selective Oxidizing Ethanol to CO_2. *Chem. Mater.* **2010**, *22*, 2395−2402.
(39) Schmidt, T. J.; Ross, P. N., Jr; Markovic, N. M. Temperature Dependent Surface Electrochemistry on Pt Single Crystals in Alkaline Electrolytes: Part 2. The Hydrogen Evolution/Oxidation Reaction. *J. Electroanal. Chem.* **2002**, *524*−*525*, 252−260.
(40) Shao, M. Palladium-Based Electrocatalysts for Hydrogen Oxidation and Oxygen Reduction Reactions. *J. Power Sources* **2011**, *196*, 2433−2444.
(41) Montero, M. A.; Fernández, J. L.; Gennero de Chialvo, M. R.; Chialvo, A. C. Characterization and Kinetic Study of a Nanostructured Rhodium Electrode for the Hydrogen Oxidation Reaction. *J. Power Sources* **2014**, *254*, 218−223.
(42) Parsons, R. The Rate of Electrolytic Hydrogen Eolution and the Heat of Adsorption of Hydrogen. *Trans. Faraday Soc.* **1958**, *54*, 1053−1063.
(43) Mistry, H.; Reske, R.; Zeng, Z.; Zhao, Z.-J.; Greeley, J.; Strasser, P.; Cuenya, B. R. Exceptional Size-Dependent Activity Enhancement in the Electroreduction of CO_2 over Au Nanoparticles. *J. Am. Chem. Soc.* **2014**, *136*, 16473−16476.
(44) Ruban, A.; Hammer, B.; Stoltze, P.; Skriver, H. L.; Nørskov, J. K. Surface Electronic Structure and Reactivity of Transition and Noble Metals. *J. Mol. Catal. A: Chem.* **1997**, *115*, 421−429.
(45) Maark, T. A.; Peterson, A. A. Understanding Strain and Ligand Effects in Hydrogen Evolution over Pd(111) Surfaces. *J. Phys. Chem. C* **2014**, *118*, 4275−4281.
(46) Crespo-Quesada, M.; Andanson, J.-M.; Yarulin, A.; Lim, B.; Xia, Y.; Kiwi-Minsker, L. UV−Ozone Cleaning of Supported Poly(vinylpyrrolidone)-Stabilized Palladium Nanocubes: Effect of Stabilizer Removal on Morphology and Catalytic Behavior. *Langmuir* **2011**, *27*, 7909−7916.
(47) van der Vliet, D.; Strmcnik, D. S.; Wang, C.; Stamenkovic, V. R.; Markovic, N. M.; Koper, M. T. M. On the Importance of Correcting for the Uncompensated Ohmic Resistance in Model Experiments of the Oxygen Reduction Reaction. *J. Electroanal. Chem.* **2010**, *647*, 29−34.
(48) Blochl, P. E. Projector Augmented-Wave Method. *Phys. Rev. B: Condens. Matter Mater. Phys.* **1994**, *50*, 17953−17979.
(49) Perdew, J. P.; Burke, K.; Ernzerhof, M. Generalized Gradient Approximation Made Simple. *Phys. Rev. Lett.* **1996**, *77*, 3865−3868.
(50) Kresse, G.; Hafner, J. *ab initio* Molecular-Dynamics for Liquid-Metals. *Phys. Rev. B: Condens. Matter Mater. Phys.* **1993**, *47*, 558−561.
(51) Herron, J. A.; Tonelli, S.; Mavrikakis, M. Atomic and Molecular Adsorption on Ru(0001). *Surf. Sci.* **2013**, *614*, 64−74.
(52) Danielson, L. R.; Dresser, M. J.; Donaldson, E. E.; Dickinson, J. T. Adsorption and Desorption of Ammonia, Hydrogen, and Nitrogen on Ruthenium (0001). *Surf. Sci.* **1978**, *71*, 599−614.
(53) Stampfl, C.; Scheffler, M. Theoretical Study of O Adlayers on Ru(0001). *Phys. Rev. B: Condens. Matter Mater. Phys.* **1996**, *54*, 2868−2872.

DOI: 10.1021/acs.jpcc.5b04587
J. Phys. Chem. C 2015, 119, 17697−17706